Check for updates

Self-assembly of water-filled molecular saddles to generate diverse morphologies and high proton conductivity†

Nyaya Prakash Pradhan, [ID] [a] Sweety Gupta,‡[a] Swapnendu Narayan Ghosh, [ID] ‡[b]
Amit Paul, [ID] *[a] Santanu Talukder [ID] *[b] and Aasheesh Srivastava [ID] *[a]

The design of single-component organic compounds acting as efficient solid-state proton conduction (SSPC) materials has been gaining significant traction in recent times. Molecular design and controlled self-assembly are critical components in achieving highly efficient SSPC. In this work, we report the design, synthesis, and self-assembly of an organic macrocyclic aza-crown-type compound, **P2Mac**, which complements synthetic ease with efficient SSPC. **P2Mac** is derived from the pyridine-2,6-dicarbox-amide (PDC) framework and contains polar amide and amine residues in its inner region, while aromatic residues occupy the periphery of the macrocycle. The crystal structure analysis revealed that **P2Mac** adopts a saddle-shaped geometry. Each **P2Mac** molecule interacts with one water molecule that is present in its central polar cavity, stabilized by a network of five hydrogen bonds. We could self-assemble **P2Mac** in a variety of unique, aesthetically pleasing morphologies such as micron-sized octahedra, hexa-pods, as well as hollow nanoparticles, and microrods. The water-filled polar channels formed through the stacking of **P2Mac** allow attaining a high proton conductivity value of 21.1 mS cm^{-1} at 27 °C under a rela-tive humidity (RH) of 95% in the single crystals of **P2Mac**, while the as-prepared **P2Mac** pellet sample exhibited about three-orders of magnitude lower conduction under these conditions. The low activation energy of 0.39 eV, calculated from the Arrhenius plot, indicates the presence of the Grotthus proton hopping mechanism in the transport process. This report highlights the pivotal role of molecular design and self-assembly in creating high-performance SSPC organic materials.

Introduction

The development of organic solid-state proton conduction (SSPC) materials holds great significance across a wide range of technical domains ranging from energy storage and conversion devices such as Proton Exchange Membrane (PEM) fuel cells, hydrogen separation and batteries to sensors and bio-medical devices.[1–5] SSPC refers to the ability of materials to facilitate the transport of protons through them, allowing for the conversion of chemical energy into electrical energy.[6] Designing efficient SSPC materials is crucial for advancing

[a]Department of Chemistry, Indian Institute of Science Education and Research Bhopal (IISER Bhopal), Bhauri, Bhopal Bypass Road, Bhopal, 462 066 Madhya Pradesh, India. E-mail: asrivastava@iiserb.ac.in
[b]Department of Electrical Engineering and Computer Science, Indian Institute of Science Education and Research Bhopal (IISER Bhopal), Bhauri, Bhopal Bypass Road, Bhopal, 462 066 Madhya Pradesh, India
†Electronic supplementary information (ESI) available. CCDC 2326935. For ESI and crystallographic data in CIF or other electronic format see DOI: https://doi.org/10.1039/d4nr00456f
‡These authors contributed equally to this work.

clean and renewable energy technologies and overcoming certain challenges related to conventional proton-conducting systems.[7,8] The current SSPC materials based on metal–organic frameworks (MOFs),[9–12] carbon–organic frameworks (COFs),[13–16] polymer electrolytes,[17–19] perovskite oxide,[20–24] *etc.* offer limited solution processability and the use of metal ions can lead to adverse environmental consequences and loss of activity upon leaching of metal ions. In this context, there is a need for developing highly efficient single-component mole-cular SSPC materials that can offer advantageous features such as light weight, improved processability, and diversification through molecular design.[25]

The single-component hydrogen-bonded organic frame-work (HOF) has also gained prominence as a potential SSPC material since the first report by Müllen *et al.*, who prepared a phosphonic acid-based HOF with a self-assembled columnar structure, displaying a consistently high proton conductivity of 3.2 mS cm^{-1} in the temperature range of 120 to 180 °C under 1 bar H$_2$O atmosphere.[26] The conductivity was ascribed to the intramolecular H-bonded network formed by phosphonic acid groups within the framework. Later, in 2016, Chen *et al.* intro-

duced a metal-free porphyrin-based single-component HOF, exhibiting a moderately high proton conductivity of 3.4×10^{-3} mS cm^{-1} at room temperature and 97% RH.[27] In a recent study, Zhang and co-workers showcased the achievement of superprotonic conductivity ($\sigma = 22.1$ mS cm^{-1}) in a HOF material by inserting DMSO as guest molecules under anhydrous conditions at 100 °C.[28] Such organic SSPC materials can benefit from exploiting supramolecular interactions such as hydrogen bonding, π–π stacking, and CH–π interactions, as well as charge transfer (CT) interactions to direct molecular self-assembly in order to create proton conducting conduits that ease the flow of H$^+$ through them.[29–31] These interactions play a crucial role in stabilizing the functional supramolecular self-assemblies.[32–34] Thus, understanding the principles underlying the self-assembly process and its impact on the resulting structural arrangement is essential for enhancing the proton conducting ability. It is evident from the literature reports that both molecular design and spatial organization of molecules play critical roles in creating efficient SSPC organic motifs. Previously, Wang *et al.* demonstrated that highly ordered nanostructures obtained through self-assembly through H-bonding and other interactions facilitate superior SSPC.[35] In this study, melamine and trimesic acid were utilized to create crystalline nanowires, where the trimesic acid acts as a proton source in the system. However, the design of single-component SSPC organic molecular materials is rather rare and holds great relevance in the realm of designing pure organic electronics.

Our group has been designing pyridine-2,6-dicarboxamide (PDC) based molecular scaffolds demonstrating diverse capabilities such as anion sensing,[36] host–guest extraction,[37] charge-transfer interactions (CTI),[38] and photoisomerization.[39] Recently, we have reported a PDC-based amphiphilic molecular clip that can efficiently co-transport both H$^+$ and Cl$^-$ ions across synthetic lipid vesicles.[40] Furthermore, we have developed a helical scaffold based on the PDC framework that can exist in two distinct forms (yellow and orange) in polar and nonpolar solvents and also shows high SSPC (up to 1.2×10^{-1} mS cm^{-1} at 95 °C and 95% RH).[41] Taking these explorations further, we aimed to create a novel compact macrocyclic system for efficient SSPC. The macrocycle named **P2Mac** (Fig. 1) is strategically designed to facilitate a more ordered and symmetrical arrangement of molecules. It contains a hydrophilic inner core comprising amide and amine –NH residues, forming a polar aza-crown-like structure that can establish a strong H-bonding network during self-assembly. Meanwhile, the outer region incorporates nonpolar aromatic residues for efficient stacking of the macrocycles to create an extended proton-transporting channel.

Results and discussion

Synthesis and crystallographic studies

The macrocycle **P2Mac** was readily synthesized in 35% yield by clipping the previously reported PDC-based precursor **P2**[40]
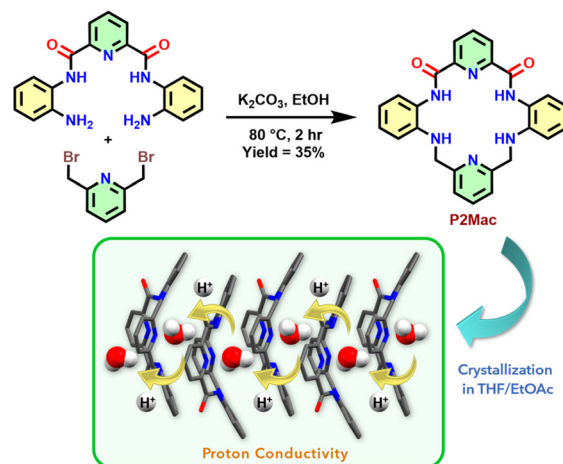
Fig. 1 Molecular design and synthetic scheme for preparing the aza-crown-like macrocycle **P2Mac** and exploring its solid-state proton conductivity.

with 2,6-bis(bromomethyl)pyridine (Fig. 1). The macrocycle was well characterized through various techniques such as mass, NMR, and single-crystal X-ray diffraction (ESI† section). In order to get structural insights into the macrocycle, single crystals of **P2Mac** were obtained by slow infusion of ethyl acetate vapors into its THF solution over the course of two to three days at 4 °C. The SC-XRD data revealed that the molecule crystallizes in the centrosymmetric monoclinic space group $P2_1/n$, with four **P2Mac** molecules per unit cell along with four water molecules. It is likely that these water molecules are either present in the solvent or are taken up by **P2Mac** molecules from the atmosphere. From the crystal structure, it was observed that the molecule adopts a saddle-shaped geometry in order to minimize the steric repulsion between the rings (Fig. 2A). The two phenyl rings present in the molecule are oriented on one side, while the two pyridine rings are oriented on the other side with a dihedral angle of 128.6° and 115.3°, respectively (Fig. S2A and S2B†). Additionally, a water molecule resides within the central cavity of each molecule, stabilized by a strong H-bonded network. We found that the presence of water molecules is crucial for stacking the macrocycles and establishing an organized and symmetrical arrangement within the crystal structure. Each water molecule formed five H-bonds with the macrocycle (O3···H1, 2.240 Å; O3···H2, 2.168 Å; O3···H3, 2.114 Å; N3···H5, 2.198 Å and N4···H5, 2.381 Å) and one with the amine –NH residue of the adjacent macrocycle (H6···N5, 2.008 Å), forming a strong H-bonded stacked water channel (Fig. 2 and S3A, S3B†). Additionally, the PDC nitrogen is engaged in intramolecular bifurcated H-bonding (H1···N1···H2) with the neighboring amide –NH groups at a distance of 2.341 Å and 2.367 Å, respectively. As a result of these interactions, the **P2Mac** molecules are stacked in a head-to-tail fashion, where PDC residues are oriented oppositely in adjacent molecules along the *b*-axis, albeit with a
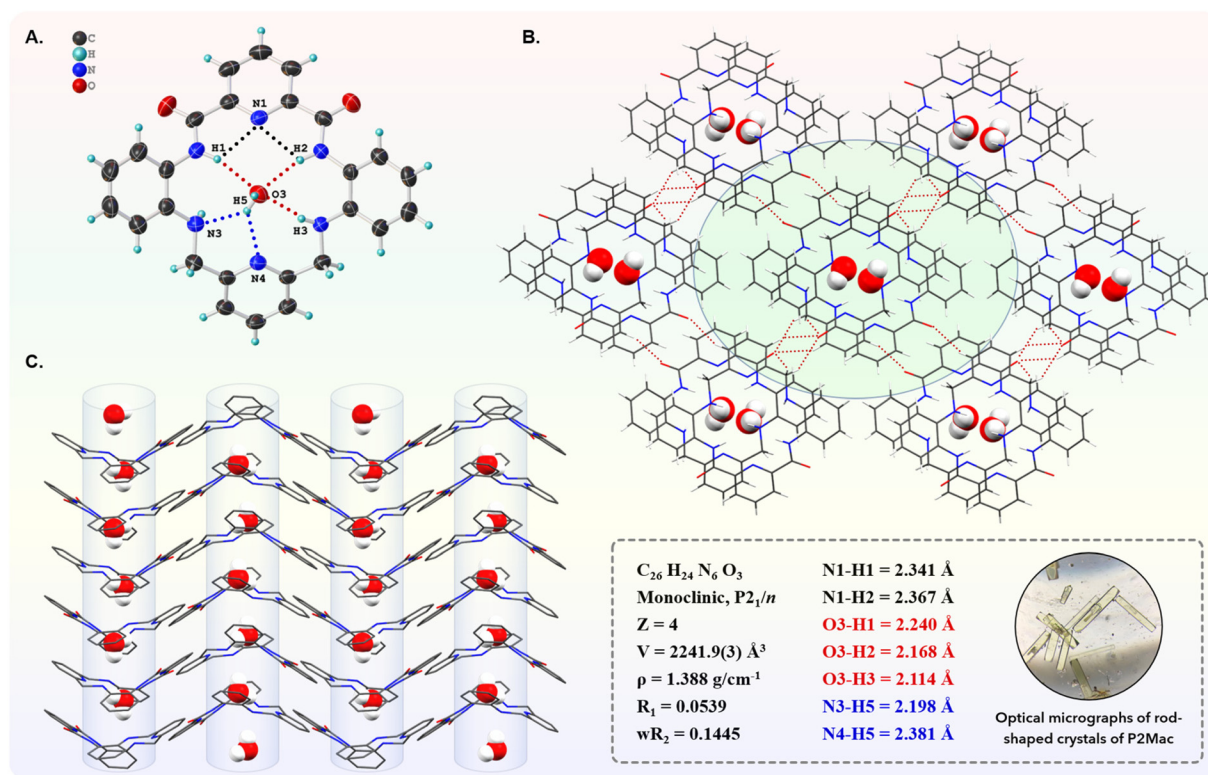
Fig. 2 SC-XRD analysis of **P2Mac** ⊃ H_2O. (A) ORTEP diagram at 50% probability showing intermolecular H-bonding interactions of **P2Mac** with H_2O. (B) Crystal packing along the *b*-axis: a top-view perspective highlighting intermolecular short-contact interactions. (C) Crystal packing along the *a*-axis illustrating the formation of linear stacks of water molecules in the crystals to form water channels for proton conduction (H atoms are omitted for clarity).

slight slip-stacked configuration, rather than being precisely aligned on top of each other (Fig. S3B†). In addition, short contacts between the amide –CO and the adjacent phenyl and pyridyl –CH were also observed, ranging from 2.4 to 2.6 Å (Fig. 2B and S3C†). These short intermolecular interactions play a crucial role in forming a more symmetrical arrangement of the molecules in all three directions. Furthermore, the addition of 2% water to the THF solution of **P2Mac** led to the formation of elongated rod-shaped crystals (Fig. S4†), which were subsequently investigated for their proton conductivity properties. A time-dependent crystal growth experiment in this solvent medium demonstrated the slow growth of the rod-shaped crystals to form elongated rods of millimeter length (Fig. S5†). The water molecules present during the crystal formation play a crucial role in the directional stacking of **P2Mac** molecules through interlinking adjacent P2Mac molecules *via* hydrogen bonds, thus setting them up for crystallization through oriented assembly. Thus, the addition of water aids in stacking the **P2Mac** molecules and promotes the directional growth of the crystals to form such elongated rods. Nonetheless, the crystals obtained in the presence of water had crystal parameters and arrangement of molecules similar to those observed for crystals obtained without any added water in the medium.

DFT calculations and EPR studies

To gain further insights into the molecular packing, DFT calculations were performed using Gaussian 09 software, utilizing the coordinates obtained from the crystal structure. We performed the energy optimization of **P2Mac** using the B3LYP/6-311G++(d,p) basis set to simulate the spatial distribution of frontier molecular orbitals (FMOs) in the molecule. The HOMO is localized on one of the phenyl residues of the molecule, whereas the LUMO lies on the PDC backbone (Fig. 3A), with a HOMO–LUMO gap of ~3.67 eV. As a result, while packing along the *b*-axis, rather than stacking directly on top of one another, **P2Mac** molecules are slip-stacked in a head-to-tail fashion with opposite orientations in order to attain spatial proximity for the HOMO and LUMO in the stacks (Fig. 3B). We performed an electron paramagnetic resonance (EPR) experiment at low temperature to verify the HOMO/LUMO charge-transfer interactions (CTI) in the molecular packing of the macrocycle.[42] The solid-state EPR experiment revealed a strong peak in the spectrum with a *g*-factor of 2.007 at 140 K (Fig. S6†). The intensity of the EPR signal was further enhanced when **P2Mac** was exposed to UV light, suggesting the formation of active radicals during the charge transfer process.
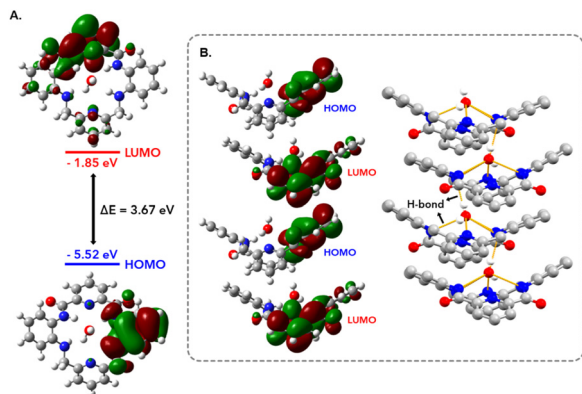
Fig. 3 (A) DFT optimized frontier molecular orbital distribution of **P2Mac** using the Gaussian 09, B3LYP/6-311G++(d,p) basis set. (B) Molecular stacking of **P2Mac** along the *b*-axis showing HOMO/LUMO interactions.

Self-assembling P2Mac into diverse morphologies

We wished to investigate how H-bonding solvent can alter the morphology of **P2Mac** self-assemblies. We varied the water/THF ratio as well as the rate of addition of THF solution of **P2Mac** (0.1 mg mL^{-1}) in the water–THF mixture to control the nucleation and growth kinetics of the self-assemblies. Here, THF would act as a good solvent for **P2Mac** while water would act as a poor solvent. By maintaining a final water/THF ratio of 50% v/v and adding the THF solution of **P2Mac** at an addition rate of 100 μL per 60 s, followed by keeping the solution undisturbed for 1 hour, we obtained uniform hollow nanoparticles with an average diameter of approximately 400 ± 25 nm (Fig. 4A and B). The hollowness of the nanoparticles is clearly

evident in the SEM and TEM images (Fig. 4B and S7†). Conversely, a rapid addition at 100 μL s^{-1} of the **P2Mac** THF solution results in the formation of microrods at a final water/THF ratio of 30% v/v (Fig. 4C and D). However, at an intermediate addition rate of 100 μL per 30 s, we managed to generate two distinct micron-sized morphologies, namely octahedron (at a final water/THF ratio of 30% v/v) and hexapod (at a 90% v/v water/THF ratio). The schematic representation of the formation of various morphologies under different water/THF ratios and addition rates is shown in Fig. 5, and a detailed procedure for creating these morphologies is provided in the ESI.† An intricate interplay of solvent–solute interaction gener-
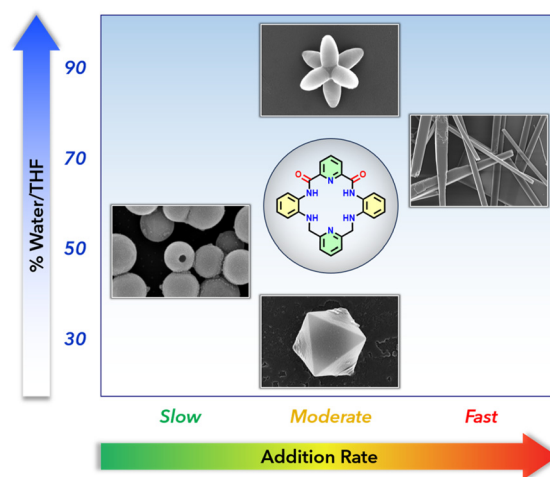
Fig. 5 Schematic illustration of the formation of diverse morphologies of **P2Mac** under different conditions.
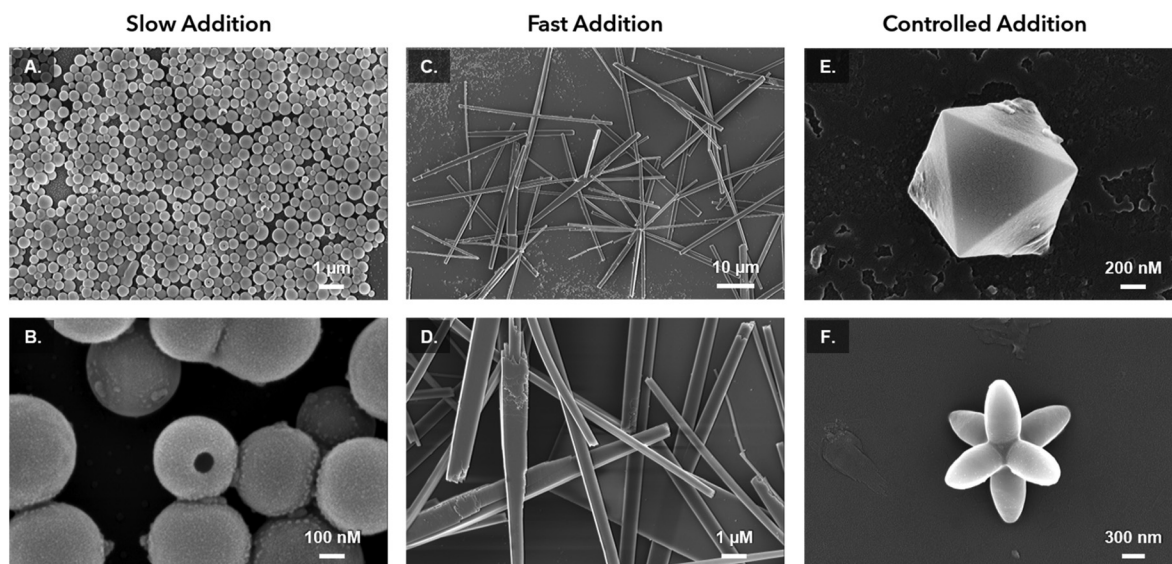
Fig. 4 SEM images of diverse morphologies at 0.1 mg mL^{-1} concentration of **P2Mac**. (A) Uniform hollow nanoparticles obtained through slow addition of **P2Mac** THF solution to produce a 50% v/v water/THF ratio. (B) Enlarged view revealing the hollowness of the nanoparticles. (C) Microrods obtained through fast addition at 30% v/v water/THF mixture. (D) Enlarged view revealing the detailed morphology of microrods. (E) Octahedra and (F) hexapods obtained through controlled addition at 30% and 90% v/v water/THF mixture, respectively.

ated these diverse morphologies through the controlled self-assembly of **P2Mac** molecules. A detailed investigation into the generation of these faceted morphologies, such as the octahedron and the hexapod, is pending and will be the subject of future studies.

Conductivity studies of P2Mac

The formation of water channels in the stacks of **P2Mac** seen in the crystal structure encouraged us to explore its solid-state proton conduction (SSPC) ability in both pellet and crystal forms. The AC proton conductivity of **P2Mac** was investigated through electrochemical impedance spectroscopy (EIS) using compressed pellets. These pellets were initially exposed to HCl vapors for 4 hours and subsequently placed inside a temperature and humidity-controlled chamber. The conductivity experiment was conducted in the frequency range of 5 MHz to 1 Hz. The semicircle obtained from the Nyquist plot was fitted according to the equivalent circuit shown in Fig. S8,† where the first semicircle that appears in the high-frequency region shows the proton conductivity value of the sample. The experiments were conducted at varying temperatures, ranging from 27 °C to 65 °C, under a relative humidity (RH) of 95%. The proton conductivity of **P2Mac** pellets, measured at 27 °C and 95% RH, was 2.17×10^{-2} mS cm^{-1}, exhibiting a notable increase to 1.79×10^{-1} mS cm^{-1} at 65 °C as illustrated in Fig. 6A. These values are remarkably high for single-component SSPC materials, which is attributed to the existence of polar self-assembled water-filled channels in **P2Mac** stacks that facilitate the migration of H$^+$ through them. However, since **P2Mac** lacks a source of protons to transmit, we kept the **P2Mac** pellets as well as the rod-shaped crystals in an environment of aqueous HCl (*ca.* 5.5 M) for 4 h to enhance the conductivity of the material. Nevertheless, no changes in the crystal structure or molecular arrangement were observed in the crystals upon such exposure, except for a color change in the pellet from light to dark yellow (Fig. S9†). To gain further insight into the mechanism of the proton transfer pathway in the pelletized **P2Mac** sample, activation energy (E_a) was calculated from the Arrhenius plot (Fig. 6B and Table S2†). The calculated E_a was found to be 0.39 eV, indicating that the proton transfer proceeds through the Grotthus mechanism.[43] Furthermore, a time-dependent stability experiment was also performed for **P2Mac** pellets at 50 °C and 95% RH, which showed that they were stable for 9 hours (Fig. 6C and Table S3†). The NMR spectra before and after conductivity measurement also demonstrated the stability of **P2Mac** (Fig. S10†).

The rod-shaped crystals of **P2Mac**, with sub-mm length, inspired us to investigate both the AC and DC conductivity of the material in its crystalline state as well (Fig. S11†). For that purpose, we fabricated a single crystal device of **P2Mac** (Fig. 6D), and the detailed fabrication procedure is outlined in section 6.4.1 of the ESI.† The AC proton conductivity of the crystal sample was measured using the EIS technique in the
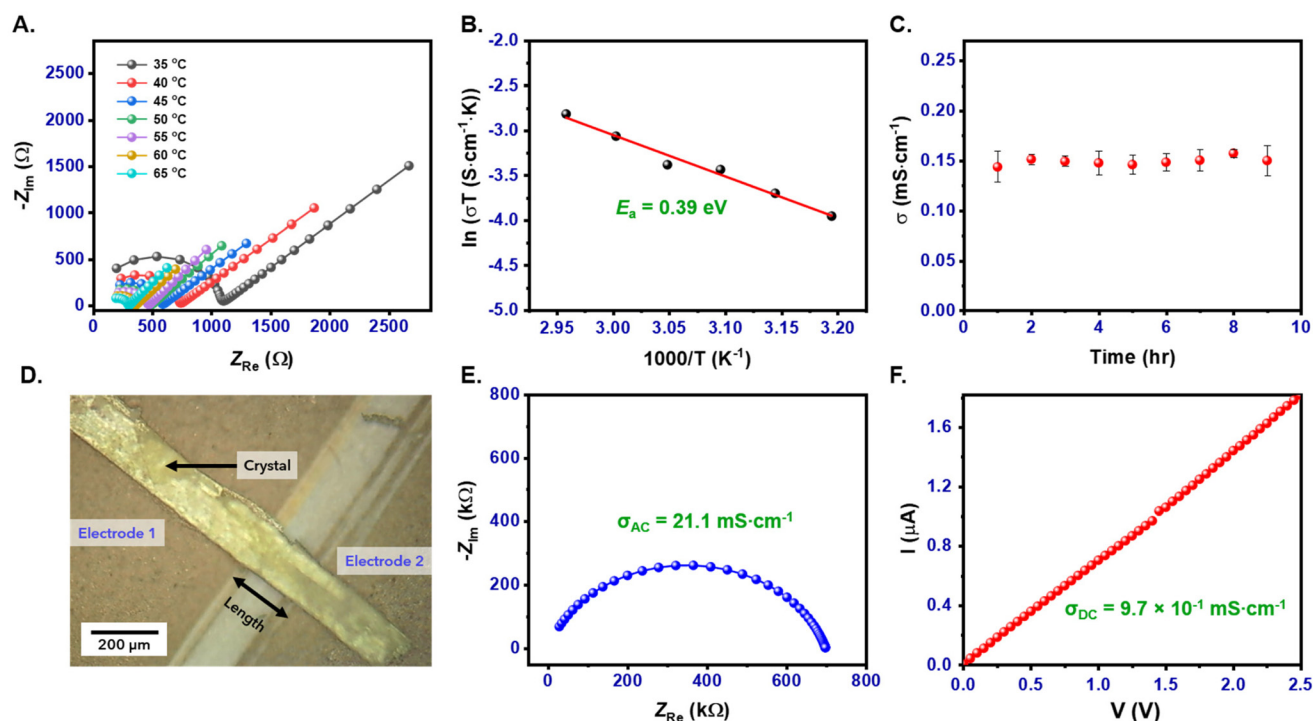
Fig. 6 Conductivity data for **P2Mac**. (A) Temperature-dependent Nyquist plots of **P2Mac** pellets at 95% RH. (B) Arrhenius plot for the calculation of activation energy (E_a). (C) Time-dependent proton conductivity plot at 50 °C and 95% RH for the pellets. (D) Optical image of a **P2Mac** crystal (L = 210 μm, W = 95.7 μm, H = 16.5 μm) connected to two electrodes for conductivity studies. (E) Nyquist plot and (F) DC I–V characteristics for single crystal conductivity measurement of **P2Mac** at 27 °C and 95% RH.

frequency range of 1 MHz to 1 kHz. At 27 °C and 95% RH, the conductivity was calculated to be 21.1 mS cm^{-1} from the first semicircle obtained from the Nyquist plot, as depicted in Fig. 6E. Compared to the pelletized sample, the crystal of **P2Mac** exhibited a remarkable three-order enhancement in proton conductivity under similar conditions. The DC current–voltage (*I–V*) characteristics of the **P2Mac** crystal showed a moderate conductivity value of 9.1×10^{-4} mS cm^{-1} at 27 °C and 50% RH. However, under high humidity conditions (95% RH), the same crystal showed a three-order increase in conductivity up to 9.7×10^{-1} mS cm^{-1} (Fig. 6F). Both the AC and DC conductivity values of the **P2Mac** crystal are comparable to those of some of the current high-performance single-component organic SSPC materials (Table S4†). The exceptionally high AC and DC conductivities observed in the crystal sample can be attributed to the highly ordered crystal packing, which reduces grain boundaries and eliminates extrinsic proton transfer across particle gaps commonly present in powder samples.

Conclusions

In conclusion, this study presents a suitably designed organic macrocycle **P2Mac** that acts as a competent single-component organic material with enhanced solid-state proton conduction (SSPC) ability. We also demonstrate how the self-assembly of **P2Mac** can be modulated in a controlled manner to produce diverse morphologies, including hollow nanoparticles, micro-rods, and micron-sized octahedra as well as hexapods through the use of different water/THF ratios and addition rates. By leveraging the molecular self-assembly of **P2Mac** in the single crystal and the spontaneous formation of a water channel in it, high SSPC values up to 21.1 mS cm^{-1} were achievable at 27 °C and 95% relative humidity. This exploration presents a useful amalgamation of molecular design and self-assembly to augment the prospects of designing efficient single-component organic proton conductors.

Conflicts of interest

There are no conflicts to declare.

Acknowledgements

References

1 K.-D. Kreuer, *Chem. Mater.*, 1996, **8**, 610–641.
2 M. M. Tellez-Cruz, J. Escorihuela, O. Solorza-Feria and V. Compañ, *Polymers*, 2021, **13**, 3064.
3 H. Iwahara, *Solid State Ionics*, 1996, **86–88**, 9–15.
4 S. Yu, M. Yang, Y. Liu and M. Liu, *Mater. Chem. Front.*, 2023, **7**, 3560–3575.
5 P. Colomban, *Solid State Ionics*, 2019, **334**, 125–144.
6 C. E. Thomas, *Int. J. Hydrogen Energy*, 2009, **34**, 6005–6020.
7 D. Vignesh and E. Rout, *Energy Fuels*, 2023, **37**, 3428–3469.
8 D. A. Medvedev, *Curr. Opin. Green Sustainable Chem.*, 2021, **32**, 100549.
9 S. Zhang, Y. Xie, R. J. Somerville, F. F. Tirani, R. Scopelliti, Z. Fei, D. Zhu and P. J. Dyson, *Small*, 2023, **19**, 2206999.
10 C. Xiao, Z. Chu, X.-M. Ren, T.-Y. Chen and W. Jin, *Chem. Commun.*, 2015, **51**, 7947–7949.
11 O. Basu, A. Das, T. Jana and S. K. Das, *ACS Appl. Energy Mater.*, 2023, **6**, 9092–9107.
12 S. S. Nagarkar, S. M. Unni, A. Sharma, S. Kurungot and S. K. Ghosh, *Angew. Chem., Int. Ed.*, 2014, **53**, 2638–2642.
13 S. Tao, L. Zhai, A. D. Dinga Wonanke, M. A. Addicoat, Q. Jiang and D. Jiang, *Nat. Commun.*, 2020, **11**, 1981.
14 L. Zhu, P. Ye, L. Zhang, Y. Ren, J. Liu, J. Lei and L. Wang, *Small*, 2024, **20**, 2304575.
15 L. Zhu, L. Zhang, Y. Ren, J. Lei, L. Wang and J. Liu, *Adv. Funct. Mater.*, 2023, 2313844.
16 W. Zou, G. Jiang, W. Zhang, L. Zhang, Z. Cui, H. Song, Z. Liang and L. Du, *Adv. Funct. Mater.*, 2023, **33**, 2213642.
17 M. N. Chai and M. I. N. Isa, *Sci. Rep.*, 2016, **6**, 27328.
18 T. Regu, C. Ambika, K. Karuppasamy, J.-H. Jeon, Y.-T. Jeong, D. Vikraman, T. A. B. Raj and H.-S. Kim, *Ionics*, 2019, **25**, 5117–5129.
19 R.-Y. Wang, S. Jeong, H. Ham, J. Kim, H. Lee, C. Y. Son and M. J. Park, *Adv. Mater.*, 2023, **35**, 2203413.
20 H. Iwahara, H. Uchida and S. Tanaka, *Solid State Ionics*, 1983, **9–10**, 1021–1025.
21 D. S. Saini, A. Ghosh, S. Tripathy, A. Kumar, S. K. Sharma, N. Kumar, S. Majumdar and D. Bhattacharya, *Sci. Rep.*, 2020, **10**, 3461.
22 C. A. Fuller, Q. Berrod, B. Frick, M. R. Johnson, M. Avdeev, J. S. O. Evans and I. R. Evans, *Chem. Mater.*, 2020, **32**, 4347–4357.
23 C. A. Fuller, D. A. Blom, T. Vogt, I. R. Evans and J. S. O. Evans, *J. Am. Chem. Soc.*, 2022, **144**, 615–624.
24 S. Fop, J. A. Dawson, D. N. Tawse, M. G. Skellern, J. M. S. Skakle and A. C. Mclaughlin, *Chem. Mater.*, 2022, **34**, 8190–8197.
25 Y.-R. Liu, Y.-Y. Chen, H.-Y. Zhao and G. Li, *Coord. Chem. Rev.*, 2024, **499**, 215516.
26 L. Jiménez-García, A. Kaltbeitzel, W. Pisula, J. S. Gutmann, M. Klapper and K. Müllen, *Angew. Chem., Int. Ed.*, 2009, **48**, 9951–9953.
27 W. Yang, F. Yang, T.-L. Hu, S. C. King, H. Wang, H. Wu, W. Zhou, J.-R. Li, H. D. Arman and B. Chen, *Cryst. Growth Des.*, 2016, **16**, 5831–5835.

28 X.-L. Wang, K.-Y. Niu, F.-F. Yang, J.-H. Wang, L. Liang and X.-M. Zhang, *Cryst. Growth Des.*, 2023, **23**, 6221–6227.

29 Z. Yang, N. Zhang, L. Lei, C. Yu, J. Ding, P. Li, J. Chen, M. Li, S. Ling, X. Zhuang and S. Zhang, *JACS Au*, 2022, **2**, 819–826.

30 S. Louie, Y. Zhong, S. T. Bao, C. Schaack, A. Montoya, Z. Jin, N. M. Orchanian, Y. Liu, W. Lei, K. Harrison, J. Hone, A. Angerhofer, A. M. Evans and C. P. Nuckolls, *J. Am. Chem. Soc.*, 2023, **145**, 4940–4945.

31 D. Shao, L. Shi, G. Liu, J. Yue, S. Ming, X. Yang, J. Zhu and Z. Ruan, *Cryst. Growth Des.*, 2023, **23**, 5035–5042.

32 J.-H. Deng, J. Luo, Y.-L. Mao, S. Lai, Y.-N. Gong, D.-C. Zhong and T.-B. Lu, *Sci. Adv.*, 2020, **6**, eaax9976.

33 X.-Z. Luo, X.-J. Jia, J.-H. Deng, J.-L. Zhong, H.-J. Liu, K.-J. Wang and D.-C. Zhong, *J. Am. Chem. Soc.*, 2013, **135**, 11684–11687.

34 H.-H. Huang, J.-H. Zhang, M. Dai, L. Liu, Z. Ye, J. Liu, D.-C. Zhong, J.-W. Wang, C. Zhao and Z. Ke, *Proc. Natl. Acad. Sci.*, 2022, **119**, e2119267119.

35 H. Wang, X. Xu, N. M. Johnson, N. K. R. Dandala and H.-F. Ji, *Angew. Chem., Int. Ed.*, 2011, **50**, 12538–12541.

36 R. Kumar and A. Srivastava, *Chem. – Eur. J.*, 2016, **22**, 3224–3229.

37 R. Kumar, H. Aggarwal, R. Bhowal, D. Chopra and A. Srivastava, *Chem. – Eur. J.*, 2019, **25**, 10756–10762.

38 R. Kumar, S. Semwal, J. Choudhury and A. Srivastava, *Chem. – Eur. J.*, 2017, **23**, 15012–15016.

39 D. Pathak and A. Srivastava, *Chem. Commun.*, 2022, **58**, 12653–12656.

40 N. P. Pradhan, K. R. Namdev and A. Srivastava, *Org. Biomol. Chem.*, 2024, **22**, 74–79.

41 H. Aggarwal, P. A. Gaikwad, A. Dahat, S. Narayan Ghosh, P. Mehra, A. Paul, S. Talukder and A. Srivastava, *Chem. – Eur. J.*, 2023, **29**, e202300019.

42 L. Sun, W. Zhu, W. Wang, F. Yang, C. Zhang, S. Wang, X. Zhang, R. Li, H. Dong and W. Hu, *Angew. Chem., Int. Ed.*, 2017, **56**, 7831–7835.

43 T. Miyake and M. Rolandi, *J. Phys.: Condens. Matter*, 2015, **28**, 023001.